Short Papers

Vision-Based Force Sensing for Nanomanipulation

Vinay Chawda and Marcia K. O'Malley

***Abstract*—In this paper, a vision-based algorithm for estimating tip interaction forces on a deflected atomic orce microscope (AFM) cantilever is described. Specifically, we propose that the algorithm can estimate forces acting on an AFM cantilever being used as a nanomanipulator inside a scanning electron microscope (SEM). The vision-based force sensor can provide force feedback in real time, a feature absent in many SEMs. A methodology based on cantilever slope detection is used to estimate the forces acting on the cantilever tip. The technique was tested on a scaled model of the nanoscale AFM cantilever and verified using theoretical estimates as well as direct strain measurements. Artificial SEM noise was introduced in the macroscale images to characterize our sensor under varying levels of noise and other SEM effects. Prior knowledge about the cantilever is not required, and the algorithm runs independent of human input. The method is shown to be effective under varying noise levels, and demonstrates improving performance as magnification levels are decreased. Therefore, we conclude that the vision-based force sensing algorithm is best suited for continuous operation of the SEM, fast scanning rates, and large fields-of-view associated with low magnification levels.**

***Index Terms*—Force measurement, image edge analysis, microscopy.**

I. Introduction

In this paper, we describe a vision-based force sensor for sensing forces acting on an atomic force microscope (AFM) cantilever being used as a nanomanipulator. The proposed vision sensor consists of a scanning electron microscope (SEM) acquiring images of the AFM cantilever in real time, which are then processed to extract and track the slope of the cantilever. Euler–Bernoulli beam theory (EBBT) is used to estimate force from the slope. We verify our scheme on a scaled model of the AFM cantilever. To produce images similar to those acquired from an SEM, we artificially introduce noise using the Artimagen library by the National Institute of Standards and Technology (NIST) [1]. Performance of the vision sensor is then analyzed under varying noise conditions and magnifications.

Nanomanipulation has been defined as the "manipulation of nanometer-size objects with nanometer-size end-effector with (sub)nanometer precision" [2]. Manipulation tasks can be of many different types such as pushing, pulling, cutting, and picking. Controlled manipulation requires sensing at the nanoscale, and the primary sensors available at the nanoscale are vision and piezoresistive force sensors. Piezoresistive sensors have been used in updating virtual reality displays for real-time fault detection and correction during pushing operations [3]. However, piezoresistive force sensors suffer from thermal and electrical noise, which places a lower bound on their resolution. Vision sensors can provide better resolution but have their own limitations depending upon the type of sensor. AFM and SEM are the two main vision sensors for nanoscale visualization.

Real-time visualization of nanomanipulation requires use of an SEM-based vision system. If an AFM is used, either imaging or nanomanipulation is possible, but they cannot be realized simultaneously. Hence, real-time visualization during nanomanipulation is not possible with an AFM alone. An added advantage of the SEM is that manipulation can be realized with multiprobe nanomanipulators that are installed within the SEM, where AFM-based manipulation is limited to single-probe interactions via the AFM cantilever. A disadvantage of using the SEM for vision-based sensing is that SEM images are prone to noise originating from the electron-emission process, mechanical drift, and vibration in the system. If force information can be reliably and robustly extracted from these raw images, a real-time force sensor can be realized.

While some SEM-based nanomanipulators offer onboard sensors to extract probe-position information, many lack sensing. We propose to mount an AFM cantilever on the tip of each SEM manipulator probe such that the cantilever deflection can be observed, which, henceforth, will be referred as the AFM–SEM approach. Therefore, it is necessary to convert information from the SEM image into contact force measurements in real time.

Requicha gives a detailed survey of nanomanipulation systems that use the AFM–SEM approach that we have chosen to use [4]. Similarly, Fahlbusch *et al.* describe several AFM–SEM-based nanomanipulations systems that incorporate nonvisual feedback (e.g., haptic or virtual reality); however, in these cases the operator remains blind during the actual operation [5]. Other groups have explored the problem of visually tracking object deformation in order to estimate interaction forces. For example, Greminger and Nelson proposed a template-matching-based algorithm to estimate the forces acting on the cantilever during nanomanipulation [6]. This method has the advantage of estimating forces acting all over the boundary of the cantilever but suffers from the requirement of prior knowledge of the cantilever shape and is not robust to changes in magnification. Liu *et al.*. also proposed a template-matching-based scheme for nano-Newton force sensing, which suffers from similar drawbacks [7]. Later, Kratochvil *et al.*. proposed a rigid body visual tracking scheme that is invariant to magnifications and is robust to noise but again requires exact knowledge of the 3-D geometry of the cantilever [8].

A vision-based force sensing technique based on cantilever slope detection is proposed which does not require any prior knowledge about shape of the cantilever and is robust to changes in magnification, SEM noise, and other effects introduced during continuous operation of an SEM. The proposed technique is verified on a scaled model of the nanoscale cantilever using force data acquired independently from a strain gage as well as theoretical estimates using tip-displacement data. Invariance of cantilever slope with scale is used to derive the force scaling factor between the nanoscale cantilever and the scaled model, which is also verified by dimensionality analysis and other approaches published in the literature. Artificial SEM noise is introduced in the images acquired from the scaled model in order to simulate various levels of SEM effects and noise. The introduction of artificial noise aids in the characterization of our algorithm's performance. This technique can also be used in the characterization of various other techniques that make use of raw SEM images.

Manuscript received May 6, 2010; revised July 20, 2010, October 17, 2010, and October 25, 2010; accepted October 26, 2010. Recommended by Technical Editor W.-J. Kim.

The authors are with the Department of Mechanical Engineering and Materials Science, Rice University, Houston, TX 77005 USA (e-mail: vinay.chawda@rice.edu, omalleym@rice.edu).

Color versions of one or more of the figures in this paper are available online at http://ieeexplore.ieee.org.

Digital Object Identifier 10.1109/TMECH.2010.2093535

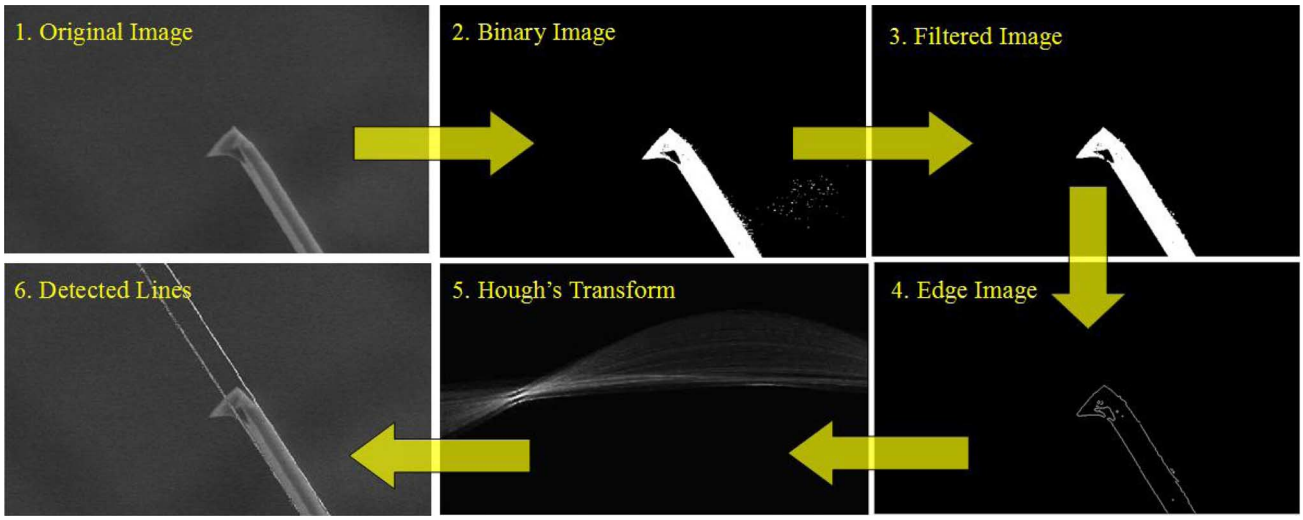

Fig. 1. Steps in vision-based detection of AFM cantilever deflection.

The rest of the paper is organized as follows. In Section II, we describe the vision-based force sensing algorithm, and its application to an SEM image of an AFM cantilever is demonstrated. In Section III, the macroscale setup is described and artificial SEM noise generation is explained. In Section IV, we compare and discuss the performance of the vision sensor under varying noise levels and magnifications with theoretical estimates as well as with the data from the strain gage. Finally, in Section V we conclude and discuss potential applications.

II. Vision-Based Force Sensing

We present an algorithm for extracting geometric information from an image of a deflecting cantilever, from which we determine forces acting on the cantilever. The primary steps of the process are as follows:

1) thresholding;
2) filtering;
3) edge detection;
4) line detection (using Hough's transform);
5) force mapping.

Fig. 1 shows the steps involved in vision-based deflection detection on a typical raw image of the AFM cantilever obtained from the SEM.

The image acquired from the camera requires some preprocessing before it can be analyzed. The acquired image is in eight-bit grayscale format, where pixels have only one attribute: intensity, which varies from 0 to 255. Most of the image processing algorithms that work on the structure of the image require conversion of the image into binary format. The process of conversion of a grayscale image into a binary image is called thresholding. In a binary image, object pixels are represented by 1s or the highest intensity possible in the image (255 in an 8-bit image) and background pixels are denoted by 0s. This type of representation retains all the structural properties of the image but loses color and texture information. The binary image obtained is usually noisy; hence, a filtering step is required for cleaning the image for further processing. Various techniques for filtering and thresholding were tested in a number of different sequences. The sequence of the techniques that provided best performance was selected and is described in the following sections.

After preprocessing, the binary image is then processed to detect deflection of the cantilever, which is then mapped to the force acting on the cantilever tip. The Canny edge operator is used to generate an edge image from the binary image. Once an edge image is obtained, Hough's transform-based line detection algorithm is used to identify the prominent lines in the image, whose slope gives the deflection of the cantilever. All these steps are discussed in detail in the following sections.

A. Thresholding

Many different methods for automatic threshold selection are available, but their performance is application dependent. Sezgin and Sankur [9] report a survey of image thresholding techniques and quantitative performance evaluation. We selected entropy-based methods because in our application, histogram or cluster-based algorithms are undesirable due to high overlap between foreground and background pixel clusters, which varies with noise levels and magnification. Also, object attribute-based and spatial methods are not suitable as they would limit the algorithm to particular shapes and structure, and robustness to changes in noise and magnification will be lost. Entropy-based methods work on the principle of maximum information transfer from grayscale to binary image. In the entropic threshold method originally proposed by Kapur *et al.*. [10], the background and foreground are considered as separate signal sources and threshold level that maximizes their combined entropy is the most optimal one as it means maximum information transfer to binary image, hence minimal loss of information. T_{opt} is the optimal threshold level, $H_f(T)$ and $H_b(T)$ are the foreground (set of pixels belonging to the cantilever) and background entropies, respectively, and $p(g)$ is the probability mass function for any grayscale level g. Equation (1) describes the process of threshold selection

$$T_{\text{opt}} = \arg\max[H_f(T) + H_b(T)] \tag{1a}$$

$$H_f(T) = \sum_{g=0}^{T} \frac{p(g)}{p(T)} \log \frac{p(g)}{p(T)} \tag{1b}$$

$$H_f(T) = \sum_{g=T+1}^{G} \frac{p(g)}{p(T)} \log \frac{p(g)}{p(T)}. \tag{1c}$$

If G is the maximum grayscale level possible in the image, for every grayscale level $T \in [0, G]$, $H_f(T)$ and $H_b(T)$ are calculated and their sum is compared with the previous value of $H_f(T) + H_b(T)$. If the new value is greater than the previous value, T_{opt} is assigned the current threshold level T else the previous value is retained. Hence, a single

pass over all possible grayscale values gives the optimal threshold value. Step 2 in Fig. 1 shows the thresholded image.

B. Filtering

After thresholding, the binary image obtained still contains some noise; hence, a filtering step is required to improve the performance of the subsequent steps. We employ a majority filter (MF) [11], which is an effective way of removing uncorrelated pixel noise. This filter efficiently deals with the psuedorandom nature of the SEM noise. An MF window is defined as a simple geometrical shape (5×5 pixel square in our case), which can encompass the biggest size noise blob expected to be removed. The center of this window is moved all over the image and at every position of the window, the whole population of the window is assigned to the class of the pixels (foreground or background) in majority in that window. Step 3 in Fig. 1 shows the image after the filtering step.

C. Edge Detection

The first step in line detection is finding edges in the image. The Canny edge operator is used for finding the edges of the cantilever in the image. The Canny edge operator takes the grayscale image as input and calculates the gradient of intensities, a vector with both magnitude and direction. The normal of the edge aligns with the direction of the gradient vector, and the magnitude gives the strength of the edge. In our case, we transfer only the strong edges to the next step for line detection, thereby introducing a secondary filtering step. Step 4 in Fig. 1 shows the detected edges.

D. Line Detection

The edge points obtained from the edge detection step are input to the Hough transform-based line detection algorithm. A line is represented in the parametric form $x\cos(\theta) + y\sin(\theta) = p$ where θ is the slope of the line, and p is the perpendicular distance from the origin. The parameter θ is varied from 0 to 2π and p is varied from 0 to the width of the image. The (θ, p) combination that contains at least two edge points denotes a line. The number of points lying on a line can be considered as a parameter denoting the degree of matching of the line with features on the original image. Step 5 in Fig. 1 shows an intensity plot between θ and p, where the intensity of each pixel is equal to the number of points lying on the line corresponding the θ, p pair. We sort the detected lines based on their prominence, defined by the number of edge points that each line contains. A threshold is selected to prevent detection of small spurious lines and save computation time. The top two lines from this sorted array are selected and checked to ensure that they are parallel to each other and are not overlapping, i.e., their slopes are within a small tolerance while perpendicular distances from each line to the origin are different. These two lines in the image, plotted over the original image, can be identified as the edges of the cantilever (Step 6). From these detected lines, we obtain the slope of the deflected cantilever.

E. Force Mapping

Since we are concerned with very small deflections (less than 10°), the Euler–Bernoulli beam equation is used to relate angular deflection of the tip to the force acting on the tip

$$\delta = \frac{\mathrm{FL}^3}{3\mathrm{EI}} \tag{2a}$$

$$\phi = \frac{\mathrm{FL}^2}{2\mathrm{EI}} \tag{2b}$$

TABLE I
DIMENSIONS OF THE NANOSCALE AND MACROSCALE CANTILEVER

Dimension	AFM Cantilever (μm)	Macroscale Cantilever (mm)
Length	240	360
Width	30	20.32
Thickness	2.7	4.064

$$F = \frac{\mathrm{Ebh}^2}{6(L-x)}\varepsilon \tag{2c}$$

where E is the Young's modulus of the cantilever, I is the second moment of area, δ is the tip displacement, ϕ is the slope at the tip, b and h are the width and thickness of the cantilever, respectively, x is the distance between strain gage and cantilever mount, F is the load acting at the cantilever tip, and ε is the strain detected by the strain gage.

III. EXPERIMENTAL METHODS

A. Macroscale Setup

A macroscale model of the AFM cantilever was designed for the implementation and validation of the vision sensor described in Section II. The experimental model was designed by linearly scaling the dimensions of the AFM cantilever 1500 times. The corresponding dimensions of the macroscale model and AFM cantilever are shown in Table I.

The macroscale model (see Fig. 2) is comprised of a cantilever, light source, camera, linear stage, and force sensing system. The cantilever was made of high-strength aluminium (Alloy 2024). A steel clamp assembly was designed to constrain the cantilever to deflect horizontally, thus negating the effects of gravity. An EO-0413 Mono USB Camera from Edmund Optics was mounted overhead to capture images of the cantilever. An acrylic pusher assembly was mounted on a micro-precision linear stage (Newport) to push the cantilever. Strain gages (EA-13-125PC-350, Vishay) were placed on the cantilever to measure strain during bending. A strain indicator (P3500, Vishay) was used to read the strain values from the gages. Camera calibration accounted for possible yaw, pitch, and roll of the camera from vertical. The Faugeras method for camera calibration was used to find a transformation matrix between deflection in a world coordinate frame and the corresponding deflection in an image coordinate frame. A calibration object was used for generation of the control points for calibration. The cantilever was initially kept in a nondeflected position while pusher was gradually moved toward the cantilever. The point where the pusher tip makes contact with the cantilever was taken as the datum position for measurement of tip displacement. The pusher was moved in steps of 1 mm while tip deflection is sensed with the vision system and strain from the strain gages was recorded for each step.

B. Force Scaling

We have considered invariance of angular deflection under geometric scaling to determine the force scaling factor between macroscale and nanoscale cantilevers. EBBT was used to estimate forces from the deflection for both macro- and nanoscales, giving a force scaling factor of 0.5285×10^6. In both macroscale and nanoscale cantilever cases, force acting on the tip can be expressed as $F = k\delta$, where k is the spring constant of the cantilever and δ is the tip displacement [12]. At the macroscale, slope of the cantilever ϕ and tip displacement δ are related by the EBBT which may not hold true at the nanoscale, and a more suitable model may be used to relate ϕ and δ. We have demonstrated a method of reliably estimating ϕ under SEM-like conditions that can give us δ, hence the force acting on the tip of the cantilever. The

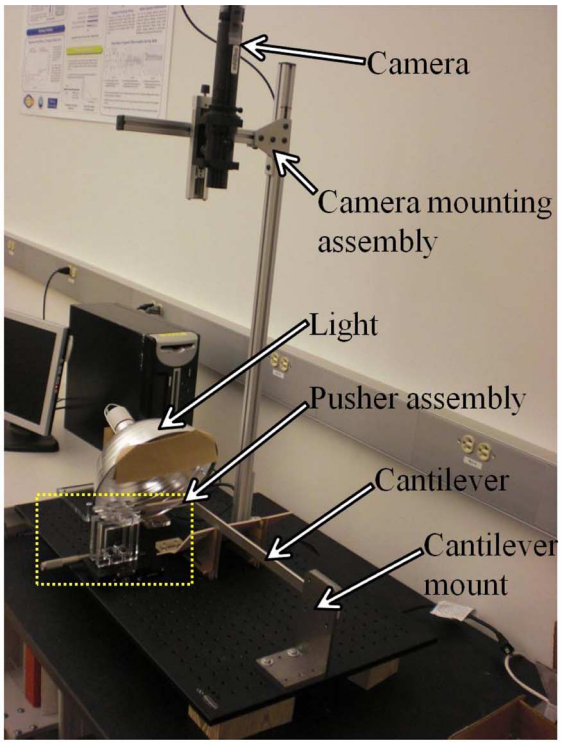

(a)

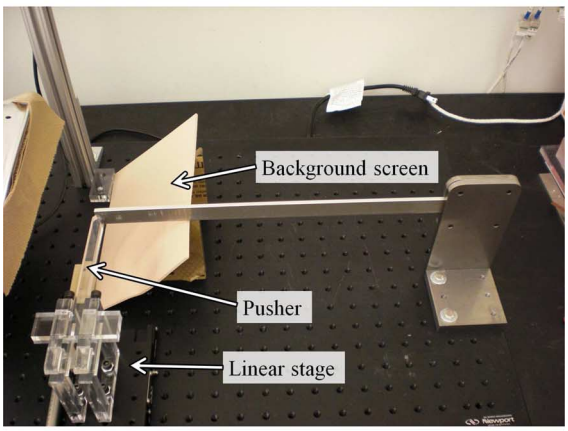

(b)

Fig. 2. Macroscale experimental setup showing the scaled cantilever beam along with the pusher mechanism and image acquisition system. (a) Macroscale experimental setup. (b) Close up view from front.

reason we used EBBT was to compare the performance of the sensor with a conventional sensor (strain gage) at the macroscale. If we were comparing with some other sensor at the nanoscale, a different model may have been used. Although we have approximated the nanoscale forces using EBBT, the qualitative trends in algorithm performance at varying magnifications and noise levels that we have observed will be unaffected by variations in the force scaling factor. Regardless of the invariance of algorithm performance with respect to force scaling factor, we have chosen to investigate two additional approaches for computing the force scaling factor to validate the value obtained by angular deflection invariance approach. Using the dimensionality analysis approach described in [13], we compute the force scaling factor to be 1.2167×10^6. The heuristic rule for calculation of the force scaling factor described in [14] under the assumption of invariance of the angular deflection breaks down to the relation obtained from the dimensionality analysis approach, hence verifying our assumption. The values obtained are, thus, comparable in magnitude to the invariance of angular deflection approach, which is used for calculation of the force scaling factor in this paper.

C. Artificial SEM Image Generation

The images obtained from the SEM contain significant noise compared to the practically noise free images from our macroscale setup. Consequently, artificial introduction of noise is required to test the vision algorithm in SEM-like conditions. Artimagen, a library for artificial charged-particle-microscopy image generation for C++ developed by NIST [15], was used to simulate SEM effects and noise. The Artimagen library allows simulation of various kinds of effects and noise introduced during SEM imaging like charging effects (also called edge effects), blur, drift, vibration, and Gaussian and Poisson noise [1]. Various effects and the corresponding models are discussed briefly in the following:

1) *Edge effects*: Edges appear brighter than the rest of the object in SEM images. This is due to progressive charge accumulation on the object by continuous bombardment with the electron beam. The charging phenomena is modeled by modulation of the grayscale values near the edge based on Monte Carlo simulation:

$$\alpha = \frac{ae^{-b/d} + c}{\mu} \tag{3}$$

where α is the noise multiplier for a particular pixel; d is the distance of the pixel from the nearest edge; μ is the center grayscale value of the image; and a,b,c are the parameters deciding the level and spread of the effect.

2) *Blur*: Due to nonideal electron beam, even in-focus images contain some amount of blur due to the nonzero size of the beam. To model this blur, the image is convolved with a circular Gaussian point spread function given by

$$G(x, y) = \frac{1}{2\pi\sigma^2} e^{-\frac{x^2+y^2}{2\sigma^2}} \tag{4}$$

where (x, y) belong to a circle centered at the pixel in consideration. Additionally, astigmatism effects are applied so that the circle is stretched by an astigmatism ratio r and rotated by an astigmatism angle ϕ.

3) *Drift and vibration*: The vibration trajectories of the sample with respect to the electron-optical column are simulated. The column and the sample are assumed stiff so only translational motion is simulated and rotation is assumed negligible, which is the case in an actual SEM. Drift is modeled as a very low frequency vibration. The vibration trajectory is constructed by superimposing an arbitrary number of harmonic oscillations with low frequencies. The parameters that can be specified are the frequency ranges, maximum amplitude, number of frequencies, pixel dead time, and line dead time.

4) *Noise*: Noise in SEM imaging can be introduced by various sources. Electron emission in an SEM is a Poisson process, and the noise introduced by the amplifiers and other electronics is Gaussian in character. The noise is dependent also on intensity due to its partial Poisson character. Hence, the noise is modeled as a mixture of Poisson and Gaussian noise.

All noise parameters are chosen so that they resemble the actual noise present in an SEM image. Four sets of noise and effects combination were chosen (see Table II) that demonstrate a progressive deterioration of image quality during the continuous operation of an SEM.

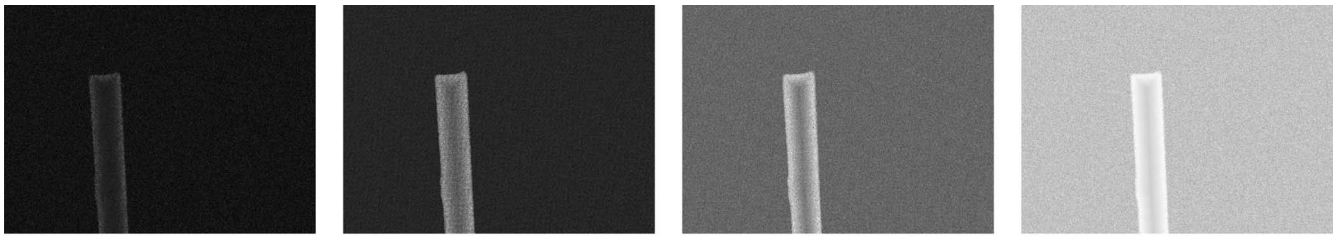

(a) (b) (c) (d)

Fig. 3. Images under different noise settings, noise magnitudes progressively increasing from Setting 1 to Setting 4. (a) Setting 1. (b) Setting 2. (c) Setting 3. (d) Setting 4.

TABLE II
SETS OF SEM NOISE AND EFFECTS PARAMETERS FORMING THE FOUR NOISE SETTINGS USED FOR TESTING ALGORITHM PERFORMANCE UNDER PROGRESSIVE DETERIORATION OF THE IMAGE QUALITY

Noise setting	Even background noise	Gaussian noise	Edge Effect			Effective charging
			a	b	c	
1	0.2	0.02	0.04	0.4	0.2	0.6
2	0.4	0.03	0.03	0.4	0.2	0.8
3	0.6	0.04	0.02	0.4	0.15	0.9
4	0.7	0.05	0.01	0.4	0.15	1

IV. RESULTS AND DISCUSSION

The force data acquired from the vision sensor were compared with both theoretical estimates using EBBT and force data from the strain gages. We chose the maximum error observed in a particular noise-magnification setting as our error measure, to give an estimate of the accuracy of the sensor. Plots in Fig. 4 show the observed error trends for different noise and magnification settings. The estimated error is the difference between deflections estimated from the tip displacement using EBBT and from the vision sensor. The measured error is the difference between deflections estimated from the strain measurements and from the vision sensor.

A. Explanation of the Observed Trends

There are several factors that affect the error trends observed during vision-based deflection detection. First, calibration error causes drift at lower magnification. The error is proportional to the distance from the projection of the optical center on the image plane. Lower magnifications mean a larger field of view, which introduces higher drift error. Second, at higher magnifications, more pixels are available per unit area. As a result, more pixels are available for edge detection (more points form a line), and minute edge details are amplified resulting in curvilinear edges.

In addition to the dependence on calibration error and magnification, the accuracy of the edge detection algorithm relies heavily on the preprocessing (thresholding and filtering) of the images, which converts the captured image into a binary image. The various kinds of SEM noise affect the various steps of the preprocessing in different ways. The even background effect reduces the contrast between the cantilever and the background, thereby making the edges blurry. Gaussian noise requires use of a MF and in the process erodes the edges of the obtained binary image. Charging effect, typical of SEM images, has the effect of brightening the surface of the cantilever. This enhances the contrast between the surface and the background and makes edges sharp. Rest of the noise and effects were constant for all images as they are either random or do not vary with continuous operation. We designed our filter to counter the Gaussian and other SEM noise, and the filter window was kept constant in the algorithm, thereby causing consistent edge degradation (in terms of absolute pixel counts) for every noise level at all magnifications.

Without noise, only hardware and preprocessing (thresholding + filtering) related factors are in play. The calibration error decreases with magnification, while error due to curvilinear edges increases with magnification. Due to proper calibration of the camera, calibration errors are minimized. Therefore, error due to curvilinear edges is the main source for the trend of increase in error with magnification observed. The increase in number of pixels available per edge improves the line detection and offsets the curvilinear effect due to increase in magnification. The trends with different levels of SEM noise closely follow the no-noise trends, denoting that effect of change in magnification is dominant over changes in levels of noise. The variation for the same magnification is very low and error is almost constant. This is because of the counteracting effects of even background and charging noise. The exception is at 24× where large portion of the image is occupied by the cantilever surface and variations are more prominent.

B. Performance of the Algorithm

The plot in Fig. 5 shows the time taken for the vision processing algorithm to calculate the deflection from the images with varying levels of noise and magnification.

As can be observed for each noise setting, computation time increases with increase in magnification except for the highest noise level (setting 4) where the trend reverses. The majority of the computation time is taken by the Hough transform-based line detection algorithm. The trend observed can be explained by the minimum number of points per line input to the line detection algorithm. The lower this number, the more lines that are detected. We pick the two lines with the highest number of points, corresponding to the edges of the cantilever. As the minimum threshold is set to a low value for lower magnifications, it causes detection of many stray lines at higher magnifications and hence adds to the computation time.

The reversal of this trend at the highest noise setting is due to a significant increase in background noise that causes detection of stray lines at lower magnifications due to a larger portion of the image being occupied by the background.

Consider the perpendicular distance of the line from the origin, p and slope of the line θ. A line is represented in terms of (p, θ) in the line detection algorithm. To search for this line, we have to parse through all possible values of (p, θ), that is $0 < p <$width of the image and $0 < \theta < 360$. The resolutions of the increments in p and θ decide the dimensions of the search space. We ran the algorithm with 0.1° resolution in θ and 1 pixel resolution in p, so we had 3600 divisions in θ and 752 divisions (image width) in the p dimension. Knowing the range of slope of the cantilever a priori can limit the search space of the algorithm for the same resolution and computation time for our software implementation could be further reduced.

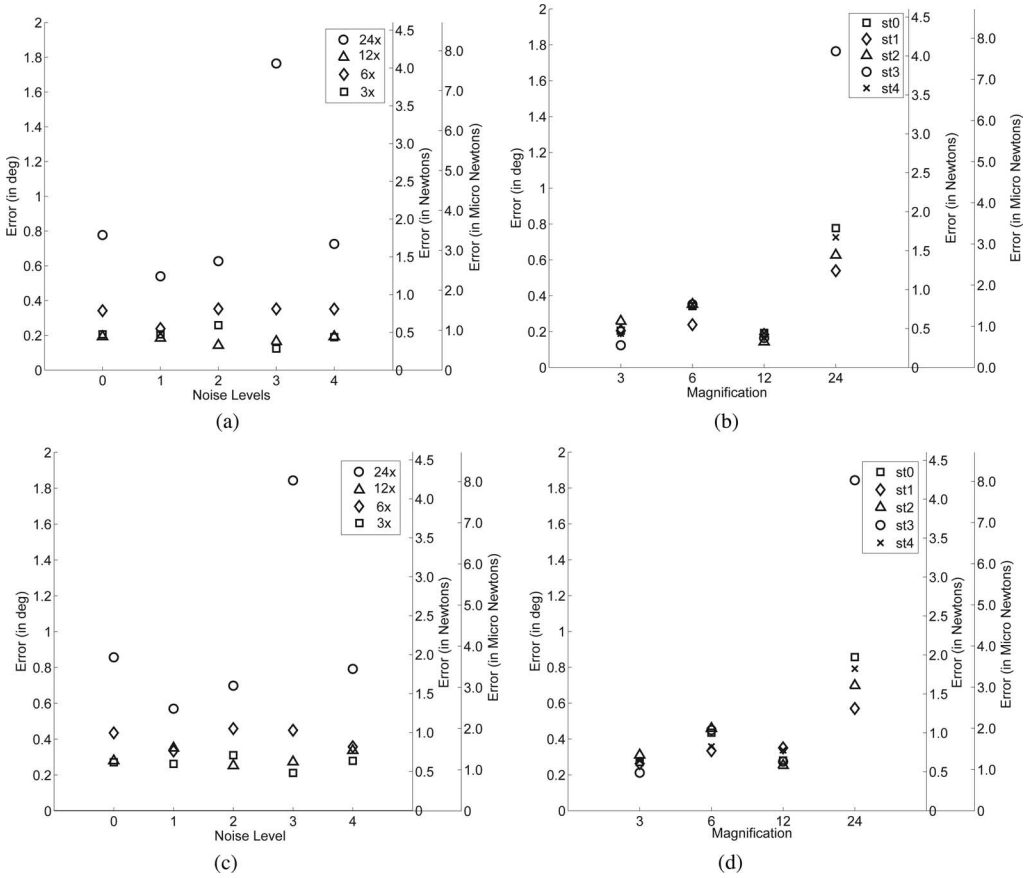

Fig. 4. Error plots showing variation with noise and magnification levels. Estimated error corresponds to the deviation from the values estimated using tip displacement and measured error corresponds to the deviation from the values measured from strain gages. (a) Estimated error: variation with noise level. (b) Estimated error: variation with magnification. (c) Measured error: variation with noise level. (d) Measured error: variation with magnification.

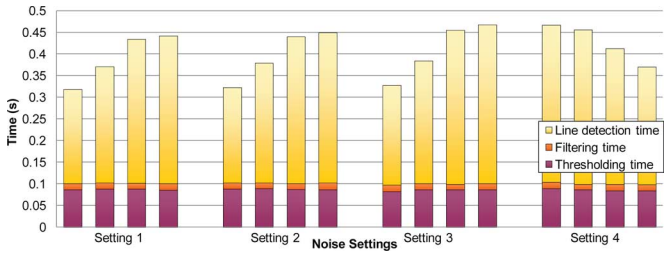

Fig. 5. Computation time for various steps of the vision-based force sensing at different noise settings, magnification increases from left to right for each setting.

With regard to the hardware used in our experiments, we have used a Windows-based system with our image processing code written in C++, with all image processing carried out in software. If we use specialized hardware for the image processing, we will further reduce the computation time. All of the library functions of the OpenCV are hardware accelerated so a faster dedicated GPU should improve the speed. Also, all computation could be transferred to GPU rather than the CPU, with the potential to save significantly the computation time as image processing algorithms are inherently parallel (doing the same thing for every pixel) [16], [17].

V. Conclusion

We have presented a vision-based force sensor for sensing forces acting on an AFM cantilever during nanomanipulation. Since our algorithm works on detection of straight edges, performance is better at lower magnifications (assuming proper calibration). Also at lower magnifications, the percentage of the area of the cantilever to the whole image is small, and hence, variations caused by different levels of noise are small. It was observed that at lower magnifications, error is low and the algorithm is robust to different levels of noise, thereby allowing use of lower magnification microscopes. The accuracy at lower magnifications is proportional to the resolution of the image, which introduces a tradeoff between scanning rate of the SEM and accuracy. At lower resolutions, higher scanning rates are possible but with loss of accuracy. The real-time performance of the algorithm is sufficient for our purpose as it matches the frame rate obtained from SEM (< 5 Hz) [18]. If the algorithm is to be used for some other application that demands faster computation, specialized hardware may be used to improve computational speed.

Acknowledgment

The authors would like to thank the assistance of Dr. A. Gupta in programming for the artificial SEM noise generation. They also would like to thank the anonymous reviewers for their constructive and insightful comments.

References

[1] P. Cizmar, A. Vladár, B. Ming, and M. Postek, "Artificial SEM images for testing resolution-measurement methods," *Microscopy Microanalysis*, vol. 14, no. S2, pp. 910–911, 2008.

[2] M. Sitti, "Survey of nanomanipulation systems," in *Proc. 1st IEEE Conf. Nanotechnol., (IEEE-NANO)*, 2001, pp. 75–80.

[3] L. Liu, Y. Luo, N. Xi, Y. Wang, J. Zhang, and G. Li, "Sensor referenced real-time videolization of atomic force microscopy for nanomanipulations," *IEEE/ASME Trans. Mechatronics*, vol. 13, no. 1, pp. 76–85, Feb. 2008.

[4] A. A. G. Requicha, "Nanomanipulation with the atomic force microscope," *Nanotechnology*, vol. 4: Information Technology II. Berlin. Germany: Vch Verlagsgesellschaft Mbh, 2008, ch. X.

[5] S. Fahlbusch, S. Mazerolle, J. Breguet, A. Steinecker, J. Agnus, R. Pérez, and J. Michler, "Nanomanipulation in a scanning electron microscope," *J. Mater. Process. Technol.*, vol. 167, no. 2–3, pp. 371–382, 2005.

[6] M. Greminger and B. Nelson, "Vision-based force measurement," *IEEE Trans. Pattern Anal. Mach. Intell.*, vol. 26, no. 3, pp. 290–298, Mar. 2004.

[7] X. Liu, K. Kim, Y. Zhang, and Y. Sun, "Nanonewton force sensing and control in microrobotic cell manipulation," *Int. J. Robot. Res.*, vol. 28, no. 8, p. 1065, 2009.

[8] B. Kratochvil, L. Dong, and B. Nelson, "Real-time rigid-body visual tracking in a scanning electron microscope," *Int. J. Robot. Res.*, vol. 28, no. 4, p. 498, 2009.

[9] M. Sezgin and B. Sankur, "Survey over image thresholding techniques and quantitative performance evaluation," *J. Electron. Imaging*, vol. 13, no. 1, pp. 146–168, 2004.

[10] J. Kapur, P. Sahoo, and A. Wong, "A new method for gray-level picture thresholding using the entropy of the histogram," *Comput. Vis. Graph. Image Process.*, vol. 29, no. 3, pp. 273–285, 1985.

[11] W. Oh and W. Lindquist, "Image thresholding by indicator kriging," *IEEE Trans. Pattern Anal. Mach. Intell.*, vol. 21, no. 7, pp. 590–602, Jul. 1999.

[12] J. Sader, J. Chon, and P. Mulvaney, "Calibration of rectangular atomic force microscope cantilevers," *Rev. Sci. Instrum.*, vol. 70, p. 3967, 1999.

[13] M. Goldfarb, "Dimensional analysis and selective distortion in scaled bilateral telemanipulation," in *Proc. IEEE Int. Conf. Robotics Autom.*, 1998, pp. 1609–1614.

[14] M. Sitti and H. Hashimoto, "Teleoperated touch feedback from the surfaces at the nanoscale: Modeling and experiments," *IEEE/ASME Trans. Mechatronics*, vol. 8, no. 2, pp. 287–298, Jun. 2003.

[15] P. Cizmar, A. Vladár, and M. Postek, "Optimization of accurate SEM imaging by use of artificial images," *Proc. SPIE*, vol. 7378, p. 737815, 2009.

[16] P. Colantoni, N. Boukala, and J. Da Rugna, "Fast and accurate color image processing using 3d graphics cards," in *Proc. Vision, Modeling, Visualization, Conf.*, Munich, Germany, 2003, vol. 133.

[17] J. Fung and S. Mann, "OpenVIDIA: Parallel GPU computer vision," in *Proc. 13th Annu. ACM Int. Conf. Multimedia*, ACM, 2005, p. 852.

[18] S. Kim, D. Ratchford, and X. Li, "Atomic force microscope nanomanipulation with simultaneous visual guidance," *ACS Nano*, vol. 3, pp. 1319–1326, 2009.